A method for experimental thermo-mechanical aging of materials submitted to concentrated solar irradiation

Yasmine Lalau[a], Olivier Faugeroux[a,*], Bernard Claudet[a], Emmanuel Guillot[a], Damien Andre[b], Marc Huger[b], Alain Proust[c], Thierry Chotard[b,*]

[a] Procédés, Matériaux et Energie Solaire (PROMES), UPR 8521. 7 rue du Four Solaire, 66 120 Font-Romeu Odeillo Via, France / Tecnosud – Rambla de la Thermodynamique, 66 100 Perpignan, France
[b] Institut de Recherche sur les Céramiques (IRCER), UMR 7315. 12 rue Atlantis, 87 068 Limoges Cedex, France
[c] MISTRAS Group SA, 27 rue Magellan, Paris CEDEX 94370, France

ABSTRACT

Concentrated Solar Technology can produce process heat, power and fuels from solar energy in the temperature range 150–1500 °C, bringing the question of the receiver ability to reliably perform over the expected lifetime. Conventional methods commonly used to assess the mechanical stability and lifetime involve in-door laboratory testing, which suffers from the fundamental inability to reproduce the real operating conditions. A previous work introduced an original experimental setup based on acoustic emission named IMPACT (*In situ* thermo-Mechanical Probe by ACoustic Tracking), designed for an in situ and passive characterization of receiver materials under harsh thermo-mechanical stresses. This paper proposes an original method, based on a modelling approach, to control the sample damage amplification with IMPACT, and assess its relevance through an experimental campaign on two selected materials (SiC and Inconel 625).

1. Introduction

Among concentrated solar technologies, solar towers appear promising candidates in the quest for producing efficiently affordable and dispatchable solar electricity because of their high concentration (up to 1000) allowing an efficient conversion of sunlight into electricity at temperature above 500 °C and their flexibility resulting in low-cost storage integration [1,2]. The solar receiver is one of the main components of solar towers; it collects the concentrated solar radiation to transmit the heat to the working fluid. Solar receivers experience high temperatures, thermal shocks and temperature gradient because the incoming solar radiation is non-homogeneous and time-variable [3]. This cyclic service may progressively lead to cumulate fatigue damage, finally resulting in the failure of the system [4–6]. It is thus fundamental to diagnose the ability of the materials to perform reliably over extended periods that define the component lifetime. The thermal accelerated aging of materials for solar receivers has been studied in the early 2000, and more recently regarding the concentrated systems [7–12]. However, the literature dealing with thermo-mechanical damage remains very scarce [13,14]. Moreover, the conventional methods involving laboratory tests are fundamentally unable to effectively reproduce the real operating conditions, raising research efforts to develop new setups [15].

A previous work introduced an original experimental setup based on acoustic emission [16] named IMPACT (In situ thermo-Mechanical Probe by ACoustic Tracking) [17], designed for an in situ and passive characterization of receiver materials under harsh thermo-mechanical stresses. A preliminary breaking test on a Silicon Carbide ceramic (SiC) sample highlighted the setup potential to detect microstructural changes and defects at an early stage in real on-sun operating conditions. As perspective of this work, the need of the design of a specific cycling method has been pointed. This paper is focused on this issue.

In this study, the samples were exposed to solar cycling at the focus of a solar concentrator, and the evolution of induced damage was studied by acoustic emission method (see Section 2.1). The advantage of this type of test is to reproduce the real operation conditions of the solar receivers, but it is difficult to predict damage because multiple stresses are applied simultaneously. To overcome this issue an original numerical approach is proposed in order to establish cycling strategies that can separate degradation mechanisms. In these strategies, the tests generate increasingly severe complex damages, but remaining similar (presence of the same types of damage). To achieve this aim, it is first necessary to know the materials properties, which are presented in Section 2.2. Then, a model is developed to describe the thermo-
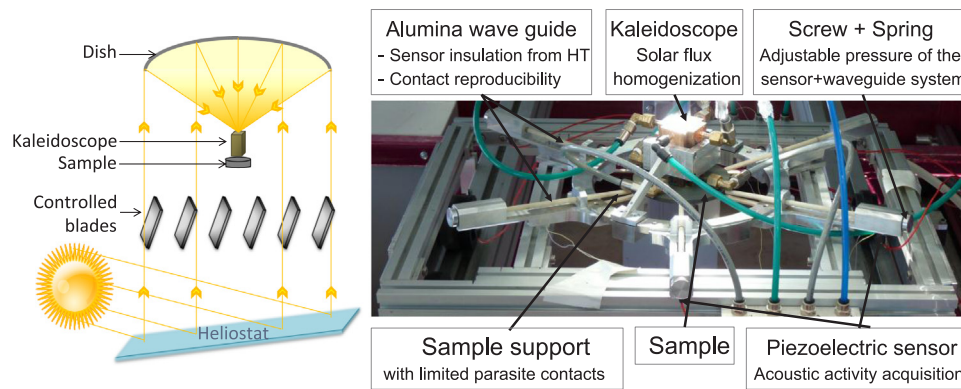

Fig. 1. Solar facility – 2 m parabolic dish (left) and acoustic setup for in situ damage monitoring of solar receiver materials placed on the solar facility focus (right).

mechanical behaviour of the samples (Section 2.3). This model is implemented in order to simulate a wide range of experimental conditions. Specific indicators are proposed in Section 3.1 in order to represent the thermo-mechanical behaviour of the samples. The numerical results thus obtained are analysed to choose tests that progressively amplify the damage of the samples (Section 3.2). These tests are carried out, and the experimental results are presented in paragraph IV.

2. Material and setup

2.1. New solar acoustic setup: IMPACT

The irradiation conditions of the solar receiver were reproduced on a few centimetre-sized samples by a 2 m diameter solar furnace (Fig. 1), part of the PROMES laboratory (France) solar facilities. The solar irradiation was reflected by a heliostat, then concentrated by a parabolic dish up to about 16 000 times (maximum concentration, 16 000 suns). A kaleidoscope homogenized the solar flux (from Gaussian to plateau distribution) delivered on the sample surface located at the kaleidoscope exit. A shutter controlled the concentrated solar irradiation on the sample surface.

This setup aims at monitoring the samples damage evolution by acoustic emission, it is presented in [17]. The acoustic emission of samples was recorded by a wide band (200–900 kHz) sensor (MICRO80) glued to a waveguide preventing them from high temperature. The type of coupling and number of sensors used to locate acoustic events was carefully selected as detailed in [17].

Acoustic emission is an in situ and passive technique for detecting defects initiation and propagation with a high sensitivity [18], and tracking their spreading. The defect apparition generates a microstructural modification, inducing elastic waves generation which propagates within the material that can be detected by a piezoelectric sensor placed on the sample surface (Fig. 2. A). This transient acoustic emission signal is defined as an *acoustic hit*. Different types of phenomena can generate the hits (localised corrosion or delamination for

instance), and are described by specific acoustic parameters depending on the signal shape (waveform): rise time, amplitude, energy, duration, frequency contents, etc. These parameters are defined in Fig. 2. B [19,20]. The acoustic signal was collected by an acquisition device is composed of a wide band (200–900 kHz) sensor (PACMICROPH-ONEμ80) above a threshold of 30 dBEA. This sensor was connected to a preamplifier and an acquisition card linked to a computer.

This technique has been applied to various domains, such as investigation of damage mechanism in composites [21,22] or ceramics [23], or characterization of fatigue cracks in metals [24]. Two approaches can be instigated to investigate the damage behaviour,

➤ Observe the real time damage evolution, by counting the cumulated hits for instance [23];
➤ Classify the damage categories, by discriminating the hits based on waveform parameters such as energy or frequency [25]. This classification can be performed by statistical analysis [21].

In this work, the materials damage evolution observed during solar cycling was assessed on paragraph IV with the help of these two approaches, the damage evolution and the damage classification.

2.2. Selected materials

The expected properties of materials used for solar tower receivers in the operating temperature range (from 500 °C to 1400 °C) are [26]:

➤ *Physical*: a high thermal conductivity favouring the heat transfer to the fluid and limiting internal gradients, and a low expansion coefficient minimizing the deformations;
➤ *Chemical*: a high corrosion and oxidation resistance;
➤ *Mechanical*: a good creep resistance and fracture toughness.

Two categories of materials can withstand the desired conditions: nickel alloys up to 800–1000 °C (Fig. 3. A) [27] and ceramics beyond 1000 °C (Fig. 3. B) [28].
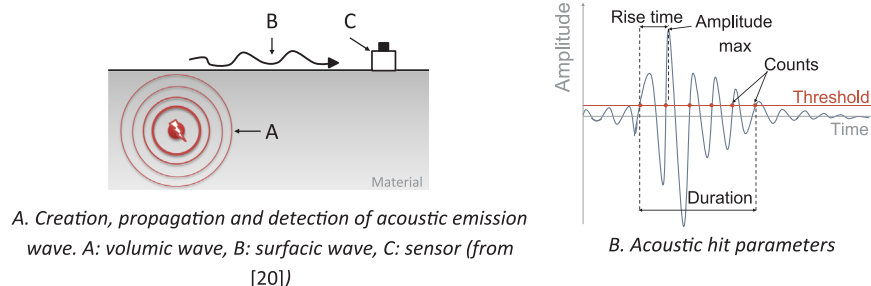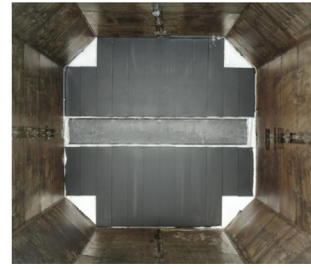

A. Creation, propagation and detection of acoustic emission wave. A: volumic wave, B: surfacic wave, C: sensor (from [20])

B. Acoustic hit parameters

Fig. 2. A. Principle of acoustic emission and B. Acoustic hit parameters.

A. Inconel metallic receiver at Invanpah tower plant (BrightSource)

B. Ceramic receiver: SiC module tested in the cavity of THEMIS tower plant [29]

Fig. 3. Examples of tubular (A) or plate (B) receivers.

Nickel alloys such as Haynes 230 or 282, and Inconel 617, 625 or 740 exhibit high creep resistance beyond 700 °C [30]. Furthermore, these alloys are easy to shape. They are referenced as resistant in high temperature and pressure environment in the *ASME Boiler and Pressure Vessel Code* [31]. Since non oxidized metals are reflective, it is mandatory to cover them with an absorptive layer such as black paint or ceramic [32,33]. However, in some solar tower configurations, the receiver wall temperature should reach at least 1000 °C to feed a gas turbine at operating temperatures (900–1300 °C): all-ceramics receivers are then relevant candidates [26].

Among the ceramics, SiC is notably emphasized for volumetric receivers [34] because of its high conductivity over 800 °C, its high solar absorptance (unfortunately associated with high emissivity, responsible for radiative heat losses [35]) and its excellent thermal and chemical stability in harsh environments [36]. Two plate prototypes have been tested up to 840 °C (rear face temperature) [37,38], but the SiC brittle behaviour and defective welding solution led to the receiver ruin in operation [29]. Other ceramic materials are under study, such as alumina, which shows a good dimensional stability, but a low solar absorptance and decreasing conductivity with temperature [39]; ultra-high temperature ceramics (UHTC) ordinarily used in aerospace applications up to 1700 °C [40]; or zirconium carbide for its natural spectral selectivity [35]. In general, material spectral selectivity can be improved by texturizing [41].

This work assesses the behaviour of one emblematic material of each category: Inconel 625 for metallic alloys and SiC for ceramics. Their properties are reported in Table 1.

The bulk density was measured by a gas pycnometer (from Micromeritics), and the thermal conductivity was determined by Laser Flash Analysis method (LFA 427 from Netzsch). The elastic properties at room temperature (Young's and shear moduli, Poisson ratio) were determined from the propagation velocity of an acoustic perturbation measured through the material sample by ultrasonic pulse echography in infinite mode, which gave results with less than 5% uncertainty. The high temperature hemispherical emissivity measurement in the wavelength range 0.6–40 μm was performed using MEDIASE facility, developed by PROMES and CNES [42,43]. The Inconel 625 sample has been oxidized at 1100 °C in air to stabilize the optical properties (heating rate: 10 °C h^{-1}, plateau: 1 h, cooling rate: 10 °C h^{-1} plus oven inertia). This temperature provided stable optical properties without deteriorating mechanical properties: before oxidation, Inconel 625 had an absorptance lower than 0.45, which is too low for efficiently absorbing solar radiation. This treatment could avoid the use of a selective coating if it withstands prolonged solar exposure. After oxidation the materials were grey in the studied wavelength range, consequently, one can consider that the emissivity is close to the absorptance [42]. Other properties (maximum stress, yield strength, and specific heat) were provided by the suppliers [44,45]: Silicon Carbide has a purely elastic behaviour, while Inconel 625 exhibits a more visco-plastic one.

The high temperature Young's modulus was determined by ultrasonic pulse echography in long bar mode [46]. As shown in Fig. 4.A, this property is quite stable at high temperature for SiC, but it significantly decreases for Inconel 625. However, the decrease is reversible: when cooling down, Young's modulus returns to its initial value. Contrarily, Silicon Carbide conductivity decreases when temperature increases (Fig. 4.B). These specific properties lead to proper damage behaviour, characterised by the original setup presented hereafter. These properties are used to build the numerical model.

2.3. Numerical model

The model was built using the multi-physical analysis code Code_Aster [47] to predict the sample thermo-mechanical dynamic behaviour in a wide range of experimental conditions (Fig. 5). The model calculated the temperature T, strain ε and stress field σ in the sample, as well as the equivalent Von Mises stress, the elastic and plastic strain, and the energy released. All these features are relevant to describe the thermo-mechanical sample behaviour, and should be considered through suitable indicators presented in the following section.

Since the setup was assumed to keep the sample free of external mechanical stresses, we considered three degrees of freedom by defining isostatic points on the sample rear face. Under these conditions, only the thermal gradients due to solar radiation induced stresses in the sample.

Fig. 5 illustrates the model approach and the thermal boundary conditions. The sample (thickness $e = 4$ mm and diameter $D = 100$ mm), was irradiated homogeneously thanks to the kaleidoscope (20 x 20 mm^2) and part of the absorbed radiation was transferred by conduction from the front to the backside. Thermal losses were given by convection and radiation on all its outer sides. The average

Table 1
SiC and Inconel 625 properties, with [*] from supplier [44,45].

Properties	Unit	T (°C)	SiC α	Inconel 625
Bulk density	kg.m^{-3}	20	3.14	8.44
Propagation velocity				
➢ Longitudinal (v$_L$)	m.s^{-1}	20	➢ 12 050	➢ 5 970
➢ Transversal (v$_T$)			➢ 7 620	➢ 3 015
Poisson ratio	–	20	0.17	0.33
Young modulus (E)	GPa	20	425	204
Shear modulus (G)	GPa	20	182	77
Maximum stress (σ$_R$) [*] (4 points bending)	MPa	20	450	965
Yield strength [*]	MPa	20		480
Thermal expansion α	(x10^{-6}) K^{-1}	500	4	13.8
		1000	4.6	15.9
Thermal Conductivity (λ)	W.m^{-1}. K^{-1}	20	180	9.8
Specific heat (Cp) [*]	J.kg^{-1}. K^{-1}	20	680	420
		500	1040	525
		1000	1180	645
Emissivity (ε)	–	1000	0.85	0.82 (oxidized)

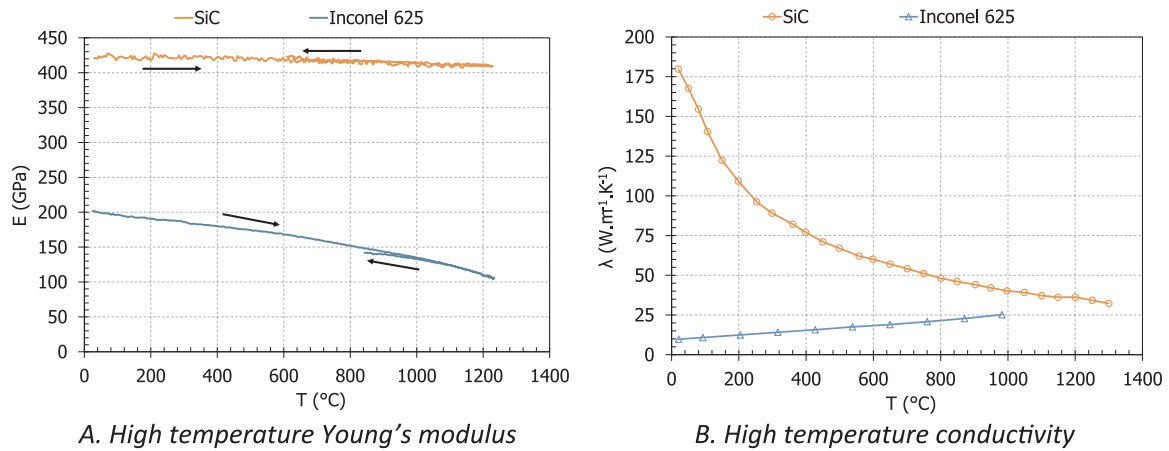*A. High temperature Young's modulus* — *B. High temperature conductivity*

Fig. 4. Temperature evolution of the properties of SiC and Inconel 625.

convective heat transfer coefficient h_{conv} was assumed equal to 20 W m^{-2} K^{-1} (a typical value for convective heat transfer with the environment), and the ambient temperature T_{amb} was fixed at 15 °C.

The thermal model was preliminary validated with an analytic steady state study of the front temperature for different solar fluxes and different materials. The given solutions presented an excellent agreement with less than 0.002% error between numerical and analytical values (Fig. 6).

Thereafter, the temperature field computed from the dynamic model has been compared to an 850 °C pre-oxidized Inconel 625 sample (50 mm diameter, 5 mm thin) experimental temperature measurement. The sample, placed at the focus of the solar concentrator, was heated using concentrated sunlight. The front face temperature was measured at the centre of the sample with a pyrometer, while the rear and side temperatures were measured using thermocouples. The results showed in Fig. 7 reveal a good agreement between numerical solution given by Code_Aster temperatures (dotted lines) and experimental temperatures (solid lines) for both the front temperature T_f (orange curve) and the back temperature T_b (green curve) when stable state is reached, after the three first cycles. The side temperature T_s is slightly overestimated in the model. These differences remains acceptable considering the approximate value of the convective coefficient considered as constant. As the model is only used to evaluate the sample behaviour in stable state, its performances are satisfying.

3. Designing relevant experimental tests by modelling

The sample thermal and mechanical responses to specified boundary conditions were simulated using the previous model to define the relevant cycling strategies for each material. The responses of the material were qualified by the thermo-mechanical indicators presented in the following paragraph. Then a sensitivity study was carried out based on non-dimensional coefficients. The analysis resulted in selecting the experimental tests that amplified the damage occurring in the sample. Several strategies have been defined, gathering the tests that should progressively increase a same damage combination.
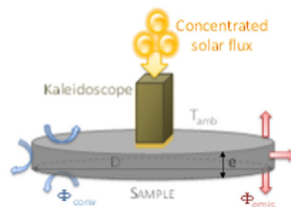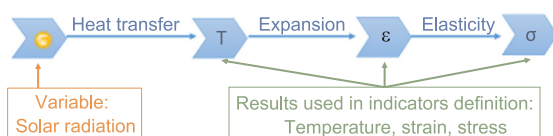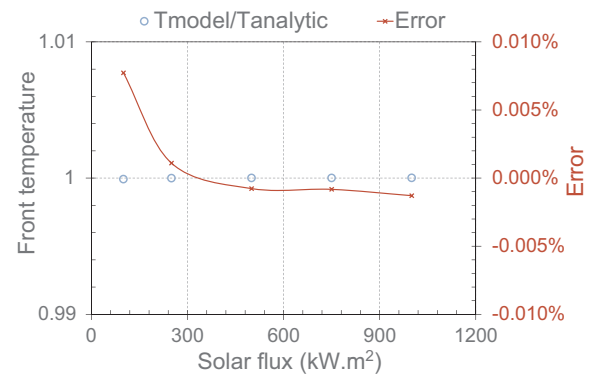

Fig. 6. Code_Aster analytic steady state validation.

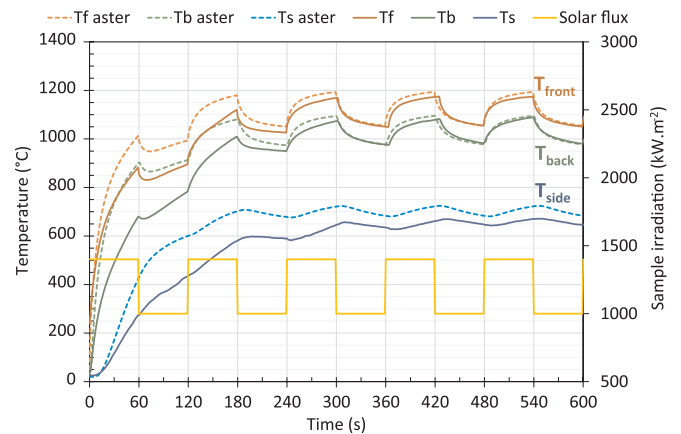**Fig. 7.** Code_Aster experimental validation. Test case: Inconel 625 Ø50 mm (pre-oxidized at 850 °C) cycling between 1000 and 1400 kW/m².

Fig. 5. A. Model approach (left) and samples thermal boundary conditions (right).

Table 2
Selected thermo-mechanical behaviour indicators.

Criterion	Parameter considered	Abbreviation and formula		Ref.
Fatigue				
Manson - Coffin	Plastic strain			[49]
		$MC = \sqrt{\Delta \varepsilon_p}$	(1)	
Smith -Watson -Tropper	Young modulus E, max. stress σ_{max}, strain amplitude $\Delta\varepsilon$	$SWT = \sqrt{E \times \sigma_{max} \times \Delta\varepsilon}$	(2)	[50]
Creep				
Zenner -Hollomon	Strain velocity $\dot{\varepsilon}$, Temperature T			[51]
		$Z = \dot{\varepsilon} \times exp\left(\frac{E_a}{RT}\right)$	(3)	
Unified damage				
Gollos - Ellyn	Energy			[49]
		$E_{TOT} = E_{plastic} + E_{elastic}$	(4)	

3.1. Thermo-mechanical indicators

These indicators have to be representative of the solar receiver materials damage induced by each cycling.

3.1.1. Selection of indicators

In a solar power plant, the material mechanical damage can be induced by two kind of mechanisms: creep by prolonged exposure to stress at high temperature, and fatigue by plant daily start up and shut down or cloud events. Creep can occur when operation temperature is about 40% of melting temperature T_m for steel, and about 50% of T_m for ceramics: the phenomenon is not critical for SiC ($T_m = 2730$ °C), but is for Inconel 625 ($T_m = 1300$ °C). Then, different damage criteria should be used for each material. According to literature, fatigue is mainly caused by stress amplitude and can be exacerbated by positive mean stress and/or high temperature. It is characterised by the plastic strain or the energy released in a cycle [48]. The durability is driven by the number of cycles. Creep is produced by exposure to rather constant stress level at high temperature, and is characterised by the strain rate, but can also be studied with energy released. Considering this, the indicators summarized in Table 2 have been determined for various boundary conditions.

A basic fatigue criterion *MC* from Manson and Coffin was studied, based on plastic strain amplitude (Equation 1) [49]. A second fatigue criterion *SWT* was also considered, taking into account the mean stress value and some temperature effect across the Young modulus (Equation 2) [50]. This criterion can also be used for SiC as it is based on the total strain and not only the plastic one. The creep criterion *Z* is based on strain rate, temperature, and activation energy (Eq. (3)) [51]. This criterion is generally presented in its logarithmic form, *log Z*, and its decrease traduce a degradation in the material creep resistance. According to Fatemi et al. [49], an energy based damage criterion E_{TOT} could unify the damage caused by the different types of loading, assumed by Eq. (4) [49].

The strain and stress values are the Von Mises values, allowing a quick comparison of the stress state of the structure. Indeed, it takes into account the tensile, compressive and shear components to give an isotropic equivalent strain and stress values.

3.1.2. Parametric study

The boundary conditions parameters have been chosen in order to amplify standard conditions but avoiding material sudden destruction, within the setup limits. The solar flux was identified as the most influent boundary condition. The solar flux density was applied in rectangular cycles, with a mean value ranging from 500 kW·m^{-2} to 1000 kW·m^{-2}, an amplitude of 150 kW·m^{-2} to 500 kW·m^{-2}, and a period between 30 s and 120 s. The maximum solar flux density at the kaleidoscope outlet was 1500 kW·m^{-2}.

These test conditions were designed to achieve receiver operation temperatures (up to about 1000 °C) and to amplify the thermal stresses typically experienced by the materials, thermal gradients being about 7 K·mm^{-1} for Inconel 625 [14] and 16 K·mm^{-1} for SiC [52] in nominal conditions. The objective of the parametric study was to investigate the influence of solar flux density variation (mean value, amplitude and period) on the materials thermo-mechanical behaviour indicators. However, the previously defined indicators present different values, units and ranges. Therefore, in order to be able to compare them, a specific non-dimensional sensitivity coefficient has been defined as follows,

$$Z_\beta^*(I) = \left| \frac{\bar{\beta}}{I_{max}} \cdot \frac{\Delta I}{\Delta \beta} \right| = \left| \frac{I \; relative \; variation}{\beta \; relative \; variation} \right| \tag{5}$$

I is the indicator, I_{max} is its maximal value and ΔI the range of possible values of *I*. β is the solar cycle parameter (mean value, amplitude or period), $\Delta\beta$ the range of possible values, and $\bar{\beta}$ the mean value within this range. The non-dimensional sensitivity coefficient mainly aims at studying the influence of parameters variation on indicators in a comparative way. Thereby, it allows comparing the relative variation of each indicator *I* due to the relative variation of each parameter β. As an example, the SWT non-dimensional sensitivity coefficient caused by amplitude variation ΔA is calculated as follows:

$$Z_A^*(SWT) = \left| \frac{A_{moy}}{SWT_{max}} \cdot \frac{\Delta SWT}{\Delta A} \right| \tag{6}$$

If $Z_A^*(SWT)$ takes large values, it means that the SWT indicator significantly varies with the solar flux amplitude. Thus, the amplitude variation will be a relevant strategy to study the damage associated to this indicator. This stimulation is selective, only this indicator varies significantly with the amplitude, if the non-dimensional sensitivity coefficients of the other indicators take low values. Finally, comparing the value of the sensitivity coefficients of the indicators for different boundary conditions results in finding a way to stimulate selectively the different types of material damages. This investigation was achieved using the numerical model previously introduced, and the results are presented in the next paragraph.

3.2. Cycling strategies

The reference case of this sensitivity study is defined by the following parameter settings: mean solar flux ϕ_m = 750 kW·m^{-2}, amplitude A = ϕ_m/2, and a period τ = 120 s. When the solar flux amplitude A is equal to 0 that means that the solar irradiation is constant.

3.2.1. Inconel 625 behaviour from thermo-mechanical model
3.2.1.1. Numerical values of temperature, strain and stress. Table 3 summarizes some illustrative results from the model calculation. The reported values correspond to the maxima reached on the sample centre, for the temperature *T*, the axial temperature gradient *AG*, the radial temperature gradient *RG*, the equivalent Von Mises strain ε_{VM}, and the equivalent Von Mises stress σ_{VM}.

3.2.1.2. Sensitivity study. The large range of calculated values

Table 3
Illustrative results from the Inconel 625 thermo-mechanical model.

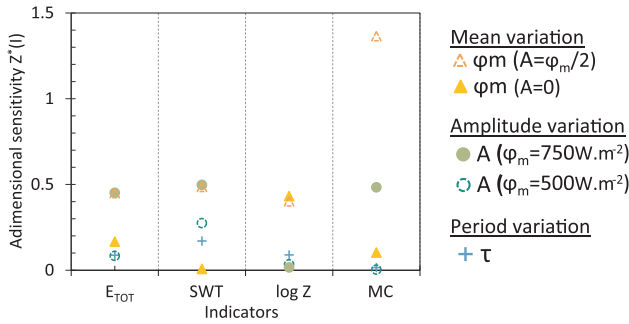|	A = 0 (plateau irradiation)		ϕ_m =750 kW·m^{-2}	
	ϕ_m = 500 kW·m^{-2}	ϕ_m = 1000 kW·m^{-2}	A = ϕ_m/3	A = ϕ_m
T (°C)	740	1044	1015	1196
AG ($K\,mm^{-1}$)	8.75	14	16	25
RG ($K\,mm^{-1}$)	5	7.9	6.5	6
ε_{VM}	5.8 x 10^{-4}	2 x 10^{-3}	1.5 x 10^{-3}	1.2 x 10^{-2}
σ_{VM} (MPa)	81	155	190	380

Fig. 8. Inconel 625 indicators sensitivity.

highlights the interest in using indicators. Fig. 8 shows the normalised sensitivity of each indicator for Inconel 625, for multiple parameters variation strategies.

The sensitivity to period τ variation is low (blue crosses), therefore, this parameter is not relevant for investigation. Its value was set to 120 s, for this value other indicators were the highest (the temperature reached in the sample centre is close to the steady state temperature).

According to Fig. 8, the mean solar flux (ϕ_m) variation (triangles) has a selective influence,

➢ For amplitude A = 0 (solid triangle) on creep indicator $log\,Z$;
➢ For amplitude A = ϕ_m/2 (dotted triangle) on all indicators with major influence on fatigue indicator MC.

The amplitude (A) variation (circles) has a selective influence:

➢ For mean solar flux ϕ_m = 750 kW m^{-2} (solid circle) on fatigue indicators SWT and MC, and on E_{TOT};
➢ For mean solar flux ϕ_m = 500 kW m^{-2} (dotted circle) on fatigue indicator SWT.

Considering these results, the thermal cycles summarized in Fig. 9 have been chosen to stimulate selectively or jointly the Inconel 625 indicators: (A) stimulates selectively log Z, (B) stimulates selectively SWT, (C) stimulates the fatigue indicators SWT, MC, and the global one E_{TOT}, and (D) stimulates the whole indicators, with specific influence on Manson-Coffin indicator.

3.2.2. SiC behaviour from thermo-mechanical model

3.2.2.1. Numerical values of temperature, strain and stress.
Table 4 summarizes some illustrative results from the model calculation on SiC. Likewise the Inconel 625 results presentation, the SiC reported values correspond to the maxima reached on the sample centre, for the temperature T, the axial temperature gradient AG, the radial temperature gradient RG, the equivalent Von Mises strain ε_{VM}, and the equivalent Von Mises stress σ_{VM}.

3.2.2.2. Sensitivity study.
Fig. 10 plots the normalised sensitivity of each indicator for SiC, for multiple parameters variation strategies. The sensitivity to period τ (crosses) is very low; consequently, this parameter is not relevant for investigation (crosses). Its value was set to 120 s to maximise other indicators. The amplitude A variation

Table 4
Illustrative results from the SiC thermo-mechanical model.

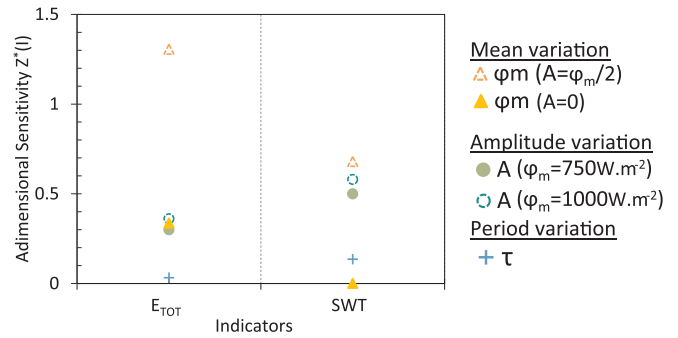|	A = 0 (plateau irradiation)		ϕ_m = 750 kW·m^{-2}	
	ϕ_m = 500 kW·m^{-2}	ϕ_m = 1000 kW·m^{-2}	A = ϕ_m/3	A = ϕ_m
T (°C)	640	805	630	783
AG (K mm^{-1})	3.5	8.4	3.7	7
RG (K mm^{-1})	2	3.2	2	3.4
ε_{VM}	1.75 x 10^{-4}	2.7 x 10^{-4}	3.57 x 10^{-4}	6.12 x 10^{-4}
σ_{VM} (MPa)	95	146	194	332

Fig. 10. SiC indicators sensitivity.

(circles) has a slight selective influence at mean solar flux ϕ_m = 1000 kW m^{-2} (dotted line) on fatigue indicators SWT.

The mean solar flux ϕ_m variation (triangles) has a selective influence at,

√ amplitude A = 0 (solid point) on unified indicator E_{TOT};
√ amplitude A = ϕ_m/2 (dotted point) on both fatigue and unified indicators SWT and E_{TOT}.
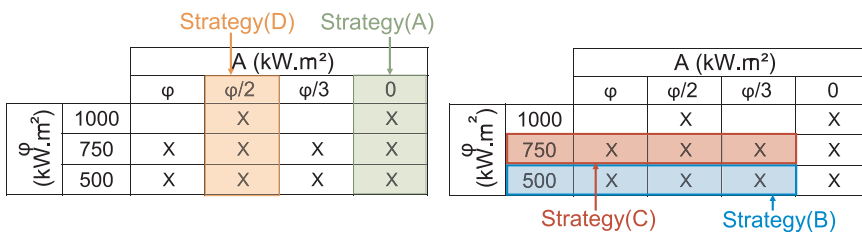
Considering these results, the thermal cycles summarized in Fig. 11 have been chosen to stimulate selectively or jointly the SiC indicators: (A) stimulates preferentially the fatigue indicator SWT, and (B) stimulates selectively the global damage indicator E_{TOT}.

4. Experimental results

The on-sun tests have been performed while recording acoustic emission samples. Each test lasts 3 hours exposure under concentrated solar flux, with a system of progressive blades opening and shut down at the cycling starting and ending; square cycles were used during test. The hits recorded during the starting and ending phases are not representative of the cyclic damage behaviour, thus they are not analysed in this work. An example of Inconel 625 cycling is shown in Fig. 12, with the front and back temperature (respectively dotted red line and green crosses), the square solar flux density (orange continuous line), and the recorded acoustic hits (blue squares). In this example, the acoustic emission is detected during the cooling phase, when the sample is mostly exposed to tensile stress.

The samples damage evolution is described by the following
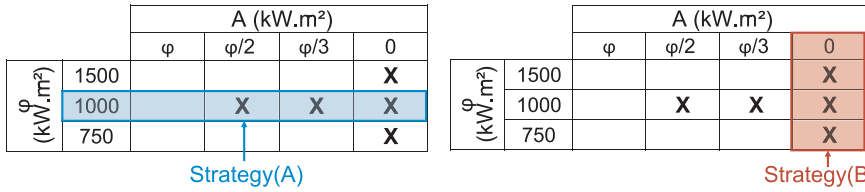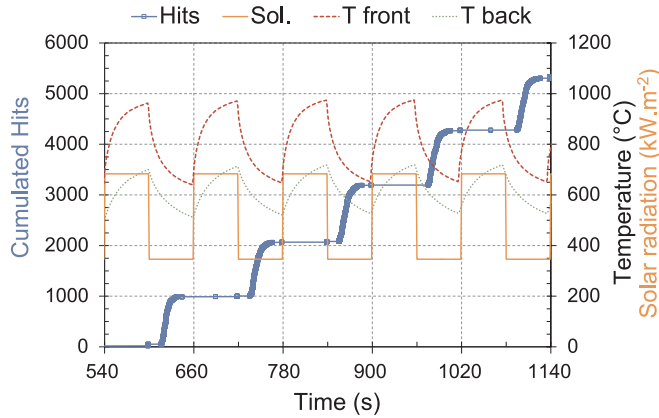
Fig. 9. Inconel 625 cycling strategies.

	A (kW.m²)						A (kW.m²)			
	φ	φ/2	φ/3	0			φ	φ/2	φ/3	0
1500 (kW.m²) φ				X		**1500** (kW.m²) φ				X
1000		X	X	X		**1000**		X	X	X
750				X		**750**				X
		Strategy(A)								Strategy(B

Fig. 11. SiC cycling strategies.

Fig. 12. Example of Inconel 625 cycling (φ_m = 500 kW·m⁻², A = 250 kW·m⁻², τ = 120 s).

acoustic parameters: activity (hits counting) for Inconel 625, and intensity (cumulated energy) for SiC, both recorded during the whole cycling. Indeed, the SiC material being a brittle ceramic, the hits are rare but energetic, cumulated energy (in attojoules) is then a more suitable parameter to scrutinize.

Fig. 13 shows the Inconel 625 and SiC damage behaviour for all constitutive tests of the designed strategies. Considering Inconel 625, the damage does not seem to progress between the different tests in strategy (A). This result suggests that creep alone is not critically influencing the samples deterioration under the studied conditions. Likewise, strategy (A) does not affect the SiC sample damage associated with cumulated energy. The fatigue solicitation at the studied solar flux intensity (1000 kW·m⁻²) is thus not relevant to observe samples deterioration. Consequently, strategies (A) were not further analysed. The following analysis focuses on the strategies for which damage evolution has been observed.

4.1. Damage evolution in Inconel 625

Fig. 14 displays the number of hits recorded in each solar cycling as a function of the indicator calculated for the corresponding cycle. These cycles are part of the previously defined strategies (B), (C) and (D).

The damages related to the tests of strategy (D) increase linearly as
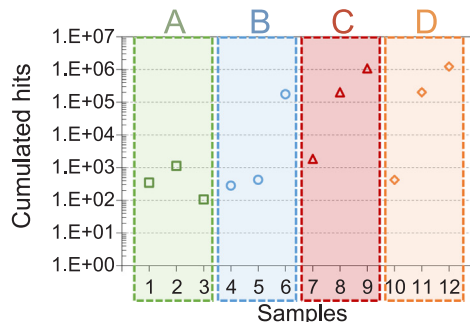
function of the indicators (except for log Z). A similar behaviour is observed for strategy (C) except for E_{TOT}, and an exponential evolution appears in strategy (B) except for MC. This connection between the experimental damage severity and the theoretical indicators reveals a damage increase that could be forecasted by the numerical model.

After the tests, some samples showed a permanent plastic deformation in their centre (as in Fig. 15) that evidences a significant (most probably critical) damage state. All the samples suffering this critical damage were exposed to solar cycles described by high indicator values beyond a threshold highlighted in Fig. 14: SWT > 180 MPa, MC > 0.012, and E_{TOT} > 100 kJ m⁻³. No threshold has been identified for log Z. No such damage state has been observed afore these thresholds. Consequently, the associated values are a first approximation of operation security values that could be more precisely defined by conducting supplementary tests characterised by indicators closed to these values.

This is an important finding; it should be possible to guarantee that critical damage will not be reached if the complex operational conditions does not overpass the indicators thresholds.
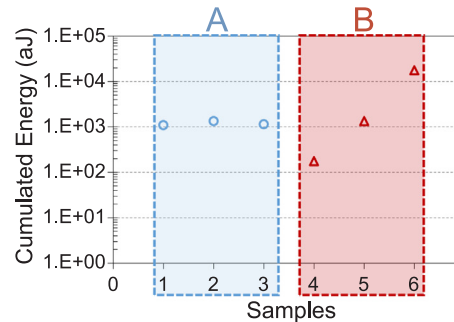
4.2. Damage evolution in SiC

Fig. 16 displays the cumulated energy recorded in each solar cycling, as function of the indicator calculated for the SiC strategy (B) cycling, E_{TOT}. The other indicator retained to describe SiC behaviour, SWT, was close to zero for the samples in strategy (B): it is consequently not relevant to study.

As for Inconel 625 tests, a damage evolution is observed with an increase of the indicator. The theoretical indicators can then effectively describe this damage evolution. It should be relevant to further investigate this relationship and its potential to manage the samples aging. However, experiments do not result in any critical damage state, therefore no indicator threshold could be defined for SiC in the range of parameters explored during this work.

5. Conclusion

An optimal strategy has been developed for the cycling of SiC and Inconel 625, based on a numerical model describing the thermo-mechanical behaviour of the material. It used previous work on solar cycling protocol [53]. This protocol has been improved, involving the

a. Cumulated hits in Inconel 625 samples

b. Cumulated energy in SiC samples

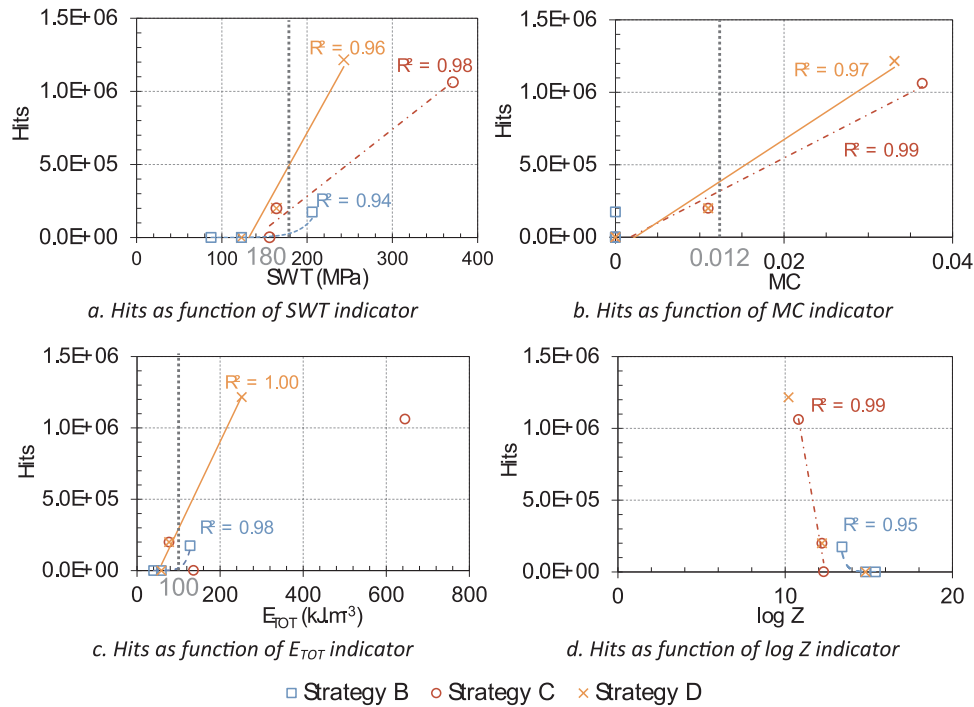**Fig. 13.** Damage behaviour of Inconel 625 (a) and SiC (b).

Fig. 14. Tests of strategies (B), (C), and (D) – Inconel 625 damage evolution (hits counting) as function of the thermo-mechanical behaviour indicators: a. SWT, b. MC, c. E_{TOT}, d. log Z.
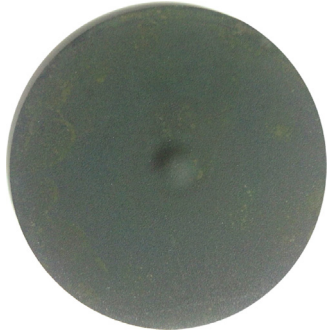

Fig. 15. Inconel 625 sample after concentrated solar cycling (φ_m = 750 kW·m^{-2}, A = φ_m, et τ = 120 s).
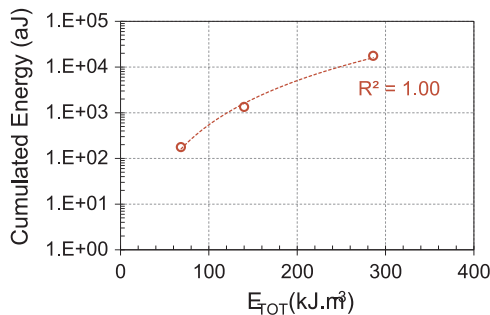

Fig. 16. Tests of strategy (B) – Linear evolution of the SiC damage (cumulated energy) as function of the thermo-mechanical behaviour indicator E_{TOT}.

following indicators:

➢ *Two fatigue criteria*: one based on the plastic strain amplitude, MC (Manson-Coffin [49]), and the other one taking into account the maximum stress, the strain amplitude and the Young's modulus, SWT (Smith – Watson – Tropper [50]);

➢ *A creep criterion*, involving the strain rate and the temperature, log Z (Zenner – Hollomon [51]);

➢ *A unified damage criterion*, corresponding to the total energy (elastic and plastic) released in the sample, E_{TOT} (Gollos – Ellyn [49]).

These indicators have been selected to describe the material response to complex thermo-mechanical loading. Their sensitivity was investigated through a parametric study. Experimental strategies (cycling conditions) were defined to obtain the greatest variation of indicators. When possible, the indicators have been selectively stimulated.

The experimental implementation of the strategies revealed different sample behaviours with respect to the indicators variation; therefore, validating the indicators relevance to describe their thermo-mechanical behaviour. The study was easier in the case of Inconel 625, which acoustic activity is greater than that of SiC because of the more numerous microstructural changes in the Inconel 625. The experimental conditions led to critical damage in Inconel 625 samples, allowing the identification of indicator threshold values very useful for operation security. That result should be adapted to solar receivers with complex geometry, in order to implement a preventive monitoring of systems during operation.

The observed trends require to be improved with a finer analysis of the types of defects that occur during cycling. Future work may attempt to, 1) identify the appearance of different damage categories, and 2) assess the IMPACT ability to monitor a damage acceleration.

Acknowledgements

References

[1] S.J. Wagner, E.S. Rubin, Economic implications of thermal energy storage for concentrated solar thermal power, Renew. Energy 61 (2014) 81–95.

[2] O. Behar, A. Khellaf, K. Mohammedi, A review of studies on central receiver solar thermal power plants, Renew. Sustain. Energy Rev. 23 (2013) 12–39.

[3] A. Boretti, S. Castelletto, S. Al-Zubaidy, Concentrating solar power tower technology: present status and outlook, Nonlinear Eng. 7 (2018).

[4] P. Rodriguez, K. Bhanu Sankara Rao, Nucleation and growth of cracks and cavities under creep-fatigue interaction, Prog. Mater. Sci. 37 (5) (1993) 403–480.

[5] W.J. Plumbridge, E.G. Ellison, Low-cycle-fatigue behaviour of superalloy blade materials at elevated temperature, Mater. Sci. Technol. 3 (9) (1987) 706–715.

[6] C.J. Lin, D.F. Socie, Fatigue behavior of ceramics under static and cyclic loading, Low. Cycle Fatigue Elasto-Plast. Behav. Mater. 3 (1992) 25–30.

[7] A. Boubault, B. Claudet, O. Faugeroux, G. Olalde, Aging of solar absorber materials under highly concentrated solar fluxes, Sol. Energy Mater. Sol. Cells 123 (2014) 211–219.

[8] A. Boubault, B. Claudet, O. Faugeroux, G. Olalde, J.-J. Serra, A numerical thermal approach to study the accelerated aging of a solar absorber material, Sol. Energy 86 (11) (2012) 3153–3167.

[9] S. Brunold, U. Frei, B. Carlsson, K. Moller, M. Kohl, Accelerated life testing of solar absorber coatings: testing procedure and results, Sol. Energy 68 (4) (2000) 313–323.

[10] M. Koehl, Durability of solar energy materials, Renew. Energy 24 (3–4) (2001) 597–607.

[11] M. Köhl, M. Heck, S. Brunold, U. Frei, B. Carlsson, K. Möller, Advanced procedure for the assessment of the lifetime of solar absorber coatings, Sol. Energy Mater. Sol. Cells 84 (1–4) (2004) 275–289.

[12] E. Setien, J. Fernández-Reche, M. Álvarez-de-Lara, M.J. Ariza, Experimental system for long term aging of highly irradiated tube type receivers, Sol. Energy 105 (2014) 303–313.

[13] A. Rojas-Morín, J. Fernández-Reche, Estimate of thermal fatigue lifetime for the INCONEL 625lCF plate while exposed to concentrated solar radiation, Rev. Metal. 47 (2) (2011) 112–125.

[14] D.K. Fork, J. Fitch, S. Ziaei, R.I. Jetter, Life estimation of pressurized-air solar-thermal receiver tubes, J. Sol. Energy Eng. 134 (4) (2012).

[15] R. Pulz, B. Rehmer, Thermal shock and thermal fatigue study of ceramic materials on a newly developed ascending thermal shock test equipment, Sci. Technol. Adv. Mater. 3 (2002) 327–334.

[16] S. Gholizadeh, Z. Leman, B.T.H.T. Baharudin, A review of the application of acoustic emission technique in engineering, Struct. Eng. Mech. 54 (6) (2015) 1075–1095.

[17] Y. Lalau, O. Faugeroux, E. Guillot, D. Andre, M. Huger, A. Proust, T. Chotard, B. Claudet, IMPACT: a novel device for in-situ thermo-mechanical investigation of materials under concentrated sunlight, Sol. Energy Mater. Sol. Cells 172 (2017) 59–65.

[18] M. Papaelias, L. Cheng, M. Kogia, A. Mohimi, V. Kappatos, C. Selcuk, L. Constantinou, C.Q.G. Muñoz, F.P.G. Marquez, T.-H. Gan, Inspection and structural health monitoring techniques for concentrated solar power plants, Renew. Energy 85 (2016) 1178–1191.

[19] C. Patapy, A. Proust, D. Marlot, M. Huger, T. Chotard, Characterization by acoustic emission pattern recognition of microstructure evolution in a fused-cast refractory during high temperature cycling, J. Eur. Ceram. Soc. 30 (15) (2010) 3093–3101.

[20] J. Roget, Émission acoustique, Tech. De. l'Ingénieur (1990) r3200.

[21] V. Carvelli, A. D'Ettorre, S.V. Lomov, Acoustic emission and damage mode correlation in textile reinforced PPS composites, Compos. Struct. 163 (2016) 339–409.

[22] S. Barré, M.L. Benzeggagh, On the use of acoustic emission to investigate damage mechanisms in glass-fibre-reinforced polypropylene, Compos. Sci. Technol. 52 (3) (1994) 369–376.

[23] T. Chotard, J. Soro, H. Lemercier, M. Huger, C. Gault, High temperature characterisation of cordierite-mullite refractory by ultrasonic means, J. Eur. Ceram. Soc. 28 (11) (2008) 2129–2135.

[24] A. Berkovits, D. Fang, Study of fatigue crack characteristics by acoustic emission, Eng. Fract. Mech. 51 (1995).

[25] L. Yang, T.T. Yang, Y.C. Zhou, Y.G. Wei, R.T. Wu, N.G. Wang, Acoustic emission monitoring and damage mode discrimination of APS thermal barrier coatings under high temperature CMAS corrosion, Surf. Coat. Technol. 304 (2016) 272–282.

[26] D.G. Morris, A. López-Delgado, I. Padilla, M.A. Muñoz-Morris, Selection of high temperature materials for concentrated solar power systems: property maps and experiments, Sol. Energy 112 (2015) 246–258.

[27] C. Pabst, G. Feckler, S. Schmitz, O. Smirnova, R. Capuano, P. Hirth, T. Fend, Experimental performance of an advanced metal volumetric air receiver for Solar Towers, Renew. Energy 106 (2017) 91–98.

[28] D.G. Morris, A. López-Delgado, I. Padilla, M.A. Muñoz-Morris, Selection of high temperature materials for concentrated solar power systems: property maps and experiments, Sol. Energy 112 (2015) 246–258.

[29] C. Leray, Etude du Comportement Thermique Et Thermomécanique Des Récepteurs Solaires Sous Haut Fluxradiatif, Université de Perpignan Via Domitia, 2017.

[30] J.A. Siefert, C. Libby, J. Shingledecker, Concentrating solar power (CSP) power cycle improvements through application of advanced materials, AIP Conf. Proc. 1734 (2016) (70030-1-70030–7).

[31] The American Society of Mechanical Engineers,Boiler & Pressure Vessel Code - Part D., 2007.

[32] C.K. Ho, A.R. Mahoney, A. Ambrosini, M. Bencomo, A. Hall, T.N. Lambert, Characterization of Pyromark 2500 paint for high-temperature solar receivers, J. Sol. Energy Eng. 136 (1) (2014) 14502.

[33] A. Soum-Glaude, A. Le Gal, M. Bichotte, C. Escape, L. Dubost, Optical characterization of TiAlNx/TiAlN y /Al $_2O$ $_3$ tandem solar selective absorber coatings, Sol. Energy Mater. Sol. Cells 170 (2017) 254–262.

[34] C.C. Agrafiotis, I. Mavroidis, A.G. Konstandopoulos, B. Hoffschmidt, P. Stobbe, M. Romero, V. Fernandez-Quero, Evaluation of porous silicon carbide monolithic honeycombs as volumetric receivers/collectors of concentrated solar radiation, Sol. Energy Mater. Sol. Cells 91 (6) (2007) 474–488.

[35] E. Sani, L. Mercatelli, F. Francini, J.-L. Sans, D. Sciti, Ultra-refractory ceramics for high-temperature solar absorbers, Scr. Mater. 65 (9) (. 2011) 775–778.

[36] Q. Li, G. Flamant, X. Yuan, P. Neveu, L. Luo, Compact heat exchangers: a review and future applications for a new generation of high temperature solar receivers, Renew. Sustain. Energy Rev. 15 (9) (2011) 4855–4875.

[37] A. Colleoni, Intensification Des Transferts En Régime Turbulent Pour Le Développement D'un Récepteur Solaire Surfacique à Haute Température En Céramique, Université de Perpignan Via Domitia, 2013.

[38] C. Leray, A. Ferriere, A. Toutant, G. Olalde, J.-.Y. Peroy, P. Chéreau, M. Ferrato, Design and Proof of Concept of an Innovative Very High Temperature Ceramic Solar Absorber, in Solar Paces.

[39] J. Karni, a. Kribus, R. Rubin, P. Doron, The 'Porcupine': a novel high-flux absorber for volumetric solar receivers, J. Sol. Energy Eng. 120 (2) (1998) 85.

[40] M. Balat-Pichelin, E. Bêche, D. Sciti, D. Alfano, Emissivity and microstructural characterization of ZrB 2-SiCfiber based UHTC at high temperature in a non-equilibrium air plasma flow, Ceram. Int. 40 (7) (2014) 9731–9742 (PART A).

[41] M. Bichotte, T. Kämpfe, W. Iff, F. Celle, S. Reynaud, T. Pouit, A. Soum-Glaude, A. Le Gal, L. Dubost, Y. Jourlin, High efficiency concentrated solar power plant receivers using periodic microstructured absorbing layers, Sol. Energy Mater. Sol. Cells 160 (2016) 328–334.

[42] M. Balat-Pichelin, J.F. Robert, J.L. Sans, Emissivity measurements on carbon-carbon composites at high temperature under high vacuum, Appl. Surf. Sci. 253 (2) (2006) 778–783.

[43] D. Hernandez, J.L. Sans, A. Netchaieff, P. Ridoux, V. Le Sant, Experimental validation of a pyroreflectometric method to determine the true temperature on opaque surface without hampering reflections, Meas. J. Int. Meas. Confed. 42 (6) (2009) 836–843.

[44] Special Metals Corporation, INCONEL alloy 625 data sheet - Publication NumberSMC-063., 2006.

[45] BOOSTEC Industries, BOOSTEC Sintered Silicon Carbide.

[46] T. Chotard, J. Soro, H. Lemercier, M. Huger, C. Gault, High temperature characterisation of cordierite-mullite refractory by ultrasonic means, J. Eur. Ceram. Soc. 28 (11) (2008) 2129–2135.

[47] EDF R&D, Code_Aster: Analysis of Structures and Thermomechanics for Studies & Research. [Online]. Available: ⟨www.code-aster.org⟩.

[48] E. Charkaluc, Fatigue Des Matériaux Métalliques: Quelques Contributions à Une Approche Dissipative, Université de Lille I, 2006.

[49] A. Fatemi, L. Yang, Cumulative fatigue damage and life prediction theories: a survey of the state of the art for homogeneous materials, Int. J. Fatigue 20 (1) (. 1998) 9–34.

[50] E. Charkaluk, a Constantinescu, An energetic approach in thermomechanical fatigue for silicon molybdenum cast iron, Mater. High. Temp. 17 (3) (2000) 373–380.

[51] J. Weertman, Zener–Stroh crack, Zener–Hollomon parameter, and other topics, J. Appl. Phys. 60 (6) (1986) 1877.

[52] J. Capeillère, A. Toutant, G. Olalde, A. Boubault, Thermomechanical behavior of a plate ceramic solar receiver irradiated by concentrated sunlight, Sol. Energy 110 (2014) 174–187.

[53] A. Boubault, Etude Du Vieillissement De Matériaux Sous Haut Flux Solaire Concentré – Application Aux Récepteurs Surfaciques Des Centrales Solaires Thermodynamiques, Université de Perpignan Via Domitia, 2013.